Available online at www.sciencedirect.com
SCIENCE DIRECT®
International Journal of Heat and Mass Transfer 47 (2004) 4045–4059
International Journal of HEAT and MASS TRANSFER
www.elsevier.com/locate/ijhmt

Ray tracing method for transient coupled heat transfer in an anisotropic scattering layer

He-Ping Tan [a,*], Hong-Liang Yi [a], Ping-Yang Wang [b], Li-Ming Ruan [a], Timothy W. Tong [c]

[a] School of Energy Science and Engineering, Harbin Institute of Technology, Harbin 150001, PR China
[b] Institute of Engineering Thermal Physics, Shanghai Jiaotong University, Shanghai 200030, PR China
[c] School of Engineering and Applied Science, The George Washington University, Washington, DC 20052, USA

Received 6 August 2003; received in revised form 2 June 2004

Abstract

A radiative transfer model for a linearly or nonlinearly anisotropic scattering medium is developed by the ray tracing method. Under specular reflection, the radiative transfer coefficients of absorbing and anisotropic scattering layer with opaque boundaries are deduced. Coupled radiative and conductive heat transfer is solved. The advantage of the method is that it only needs to disperse spatial position, but not solid angle. A comparison of the present results with the previous results shows that the radiative transfer coefficients of an anisotropic scattering slab are correct. The influence of optical thickness, surface emissivity, spectrum characteristics, albedo, and boundary conditions on the transient temperature and the heat flux distribution are analyzed. According to analyzed results of linear scattering and nonlinear scattering, it is found that the ratio of two-dimensionless heat fluxes with two different scattering phase functions is a monotone function of optical thickness. It can be used as a benchmark to verify the results.

Keywords: Coupled radiative and conductive heat transfer; Opaque boundaries; Radiative transfer coefficients; Anisotropic scattering; Scattering phase functions

1. Introduction

Radiative heat transfer in a semi-transparent medium with particles has played an important role in engineering applications [1–4]. Without taking into account scattering, the emission and absorption of radiant energy of particles often result in serious errors for total heat transfer. In fact, the radiative properties of some particles show strong characteristics of anisotropic scattering, so that it is necessary to carry out a study on radiative transfer in absorbing-emitting-anisotropic scattering media [5–12].

Busbridge and Orchard [5] gave the analytic solution of radiative transfer in a one-dimensional anisotropic scattering medium, Machali and Madkour [10], Maruyama [11] studied the same problem by means of Projection Method and REM^2, respectively. Liu and Dougherty [12] studied one-dimensional semi-infinite anisotropic scattering medium by the principle of superposition as well as Ambarzumian's method. Yuen and Wong [7], Tsai and Lin [8], Siewert [9] studied the coupled radiative-conductive steady-state heat transfer in an anisotropic scattering semi-transparent medium.

Radiative heat transfer in the participating media depends on spatial solid angle and wavelength besides spatial location. The spectral properties are simulated by the following three methods. (1) The surface and the medium are assumed to be gray. (2) The average equivalent weight parameter, e.g. Rosseland average

* Corresponding author. Tel.: +86-451-86412028; fax: +86-451-86221048.
E-mail addresses: tanheping77@yahoo.com.cn (H.-P. Tan), hongliang_yi@sina.com (H.-L. Yi).

0017-9310/$ - see front matter © 2004 Elsevier Ltd. All rights reserved.
doi:10.1016/j.ijheatmasstransfer.2004.06.007

Nomenclature

RTC radiative transfer coefficient
RTE radiative transfer equation
A_{k,T_i} $\int_{\Delta\lambda_k} I_{b,\lambda}(T_i)\,d\lambda / \int_0^\infty I_{b,\lambda}(T_i)\,d\lambda$, fractional spectral emissive power of spectral band $\Delta\lambda_k$ at nodal temperature T_i
C specific volume heat capacity, $J\,m^{-3}\,K^{-1}$
$[F^p(z)]$ radiative transfer functions (Eqs. (5)–(7))
h_1, h_2 convective heat transfer coefficient at surfaces of S_1 and S_2, respectively, $W\,m^{-2}\,K^{-1}$
H_1, H_2 convection–radiation parameter, $H_1 = h_1/\sigma T_{rf}^3$ and $H_2 = h_2/\sigma T_{rf}^3$, respectively
L thickness of slab, m
k thermal conductivity of media, $W\,m^{-1}\,K^{-1}$
N_P $k/(4\sigma T_{rf}^3 L)$, conduction–radiation parameter
NB total number of spectral bands
NM total number of control volumes of slab
$n_{m,k}$ spectral refractive index of slab
q^r heat flux of radiation, $W\,m^{-2}$
S_u, S_v boundary surfaces, S_1 or S_2, respectively
$(S_uS_v)_k$, $(S_uV_j)_k$, $(V_iV_j)_k$ radiation transfer coefficients of surface vs surface, surface vs volume, and volume vs volume in nonscattering media relative to the spectral band $\Delta\lambda_k$
$[S_uS_v]_k$, $[S_uV_j]_k$, $[V_iV_j]_k$ radiation transfer coefficient of surface vs surface, surface vs volume, and volume vs volume in isotropic or anisotropic scattering media relative to the spectral band $\Delta\lambda_k$
S_1, S_2 boundary surfaces (Fig. 1)
$S_{-\infty}$, $S_{+\infty}$ black surfaces representing the surroundings
T absolute temperature, K
T_{g1}, T_{g2} gas temperatures for convection at $X = 0$ and 1, K
T_{rf} reference temperature, K
T_0 uniform initial temperature, K
t physical time, s
t^* dimensionless time, $(4\sigma T_{rf}^3/CL)t$
t_s^* steady-state dimensionless time
X dimensionless coordinate in direction across layer, $X = x/L$
$x_{1,i}$ normal distance of ray transfer between both subscripts, m
z the normal distance of ray transfer, m
α_k spectral absorption coefficient of slab, m^{-1}
Δt, Δt^* time interval and dimensionless time interval, respectively
Δx spacing interval between two nodes, m
ε_k spectral emissivity of surface
ζ amount of the control-volume per optical thickness, $\zeta = NM/\tau_o$
η $1 - \omega$
Θ dimensionless temperature, $(T - T_0)/(T_{rf} - T_0)$
θ_i, θ incident, scattering included angle between the ray and the x-axis
κ_k spectral extinction coefficient of slab, m^{-1}
λ wavelength, μm
ρ_k spectral reflectivity of surface
σ Stefan–Boltzmann constant $= 5.6696\times10^{-8}$ $W\,m^{-2}\,K^{-4}$
$\sigma_{s,k}$ spectral scattering coefficient of slab, m^{-1}
τ_o κL, optical thickness of slab
Φ scattering phase function
Φ_i^r radiative heat source of the control-volume i
ω_k $\sigma_{s,k}/(\sigma_{s,k} + \alpha_k)$, spectral single-scattering albedo of slab

Subscripts
a absorbed quotient in the overall radiative heat transfer coefficient
ie, iw right and left interface of control volume i (Fig. 1)
k relative to spectral band $\Delta\lambda_k$
s scattered quotient in the overall radiative heat transfer coefficient
S_1, S_2 refer to the boundary surfaces S_1 and S_2, respectively
1, 2 refer to the boundary surfaces S_1 and S_2, respectively
$-\infty$, $+\infty$ refer to the black surfaces $S_{-\infty}$ and $S_{+\infty}$, respectively

Superscripts
1st, 2nd,... the first-order scattering, the second-order scattering, ..., respectively.
b, f, t incidence radiation from negative, positive and both direction relative to the x-axis, respectively, for RTC only
h, q backward scattering and forward scattering relative to the incident direction, respectively, for the radiative transfer functions only
m, $m+1$ time step
p z, q, h
r refer to radiation
s specular reflection
z emitting or isotropic scattering

absorbing coefficient is used to replace the spectra selective radiative parameters. (3) The spectral band model is used to simulate the spectral characteristics of the medium and surface.

This paper is a continuation of the authors' previous work [13–17]. Ref. [13] investigated coupled heat transfer in single layer media without scattering; Ref. [14] investigated combined heat transfer in single layer media with isotropic scattering; Ref. [15] examined couple heat transfer in two-layer media with isotropic scattering; Refs. [16,17] examined combined heat transfer in three-layer media with isotropic scattering. On the basis of those papers, ray-tracing method is extended to the radiative transfer through a linearly or nonlinearly anisotropic scattering medium. The radiative transfer coefficients (RTCs) of an anisotropic scattering medium slab with two opaque boundaries are deduced under specular reflection. The advantage of the method is that it only needs to disperse spatial position, and the integral over solid angle is calculated directly. Transient coupled radiative and conductive heat transfer is solved by the nodal analysis method in combination with the spectral band model.

2. Discrete model of space zone

A semi-transparent slab, thickness is L, as shown in Fig. 1. The slab is located between two black surfaces $S_{-\infty}$ and $S_{+\infty}$, which indicate the environment of temperatures $T_{-\infty}$ and $T_{+\infty}$, respectively. The slab is divided into $NM+2$ nodes along its thickness and denoted by i. Here, $i=1$ and $i=NM+2$ represent surfaces S_1 and S_2, respectively.

Considering transient coupled radiation and conduction, between the time intervals t and $t+\Delta t$, the fully implicit discrete energy equation of control volume i is obtained as

$$C\Delta x\frac{\left(T_i^{m+1}-T_i^{m}\right)}{\Delta t} = \frac{k_{ie}^{m+1}\left(T_{i+1}^{m+1}-T_i^{m+1}\right)+k_{iw}^{m+1}\left(T_{i-1}^{m+1}-T_i^{m+1}\right)}{\Delta x}+\Phi_i^{r,m+1} \tag{1}$$

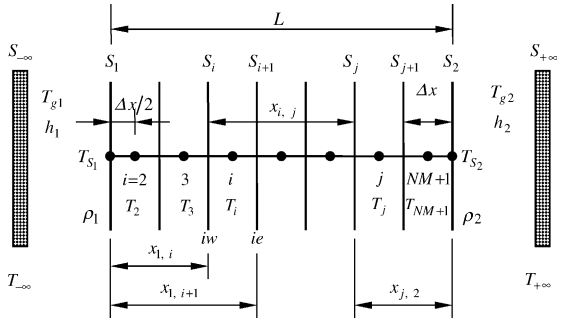

Fig. 1. Discrete model of space zone.

The extinction coefficient κ, absorption coefficient α, scattering coefficient σ_s, refractive index n_m and surface reflectivity ρ, which vary with the wavelength, are approximately simplified in a series of rectangular spectral band. The total number of spectral bands is NB and subscript k indicates the kth region of the band model. On the basis of the nodal analysis method [18], the radiative source of control volume i can be expressed as [13]:

$$\Phi_i^{r}=q_{ie}^{r}(T)-q_{iw}^{r}(T)=q_{ie}^{r}(T)-q_{(i-1)e}^{r}(T) \tag{2}$$

When boundary surfaces S_1 and S_2 are opaque, the radiative heat flux through the interface 'ie' between the nodes i and $i+1$ can be expressed as:

$$\begin{aligned} q_{ie}^{r}=\sigma\sum_{k=1}^{NB}n_{m,k}^2\Bigg\{&\varepsilon_{2,k}[S_2S_1]_k^{s}A_{k,T_{S_2}}T_{S_2}^4-\varepsilon_{1,k}[S_1S_2]_k^{s}A_{k,T_{S_1}}T_{S_1}^4\\ &+\sum_{j=i+1}^{NM+1}\sum_{l=2}^{i}\left([V_jV_l]_k^{s}A_{k,T_j}T_j^4-[V_lV_j]_k^{s}A_{k,T_l}T_l^4\right)\\ &+\sum_{j=2}^{i}\left(\varepsilon_{2,k}[S_2V_j]_k^{s}A_{k,T_{S_2}}T_{S_2}^4-[V_jS_2]_k^{s}A_{k,T_j}T_j^4\right)\\ &+\sum_{j=i+1}^{NM+1}\left([V_jS_1]_k^{s}A_{k,T_j}T_j^4-\varepsilon_{1,k}[S_1V_j]_k^{s}A_{k,T_{S_1}}T_{S_1}^4\right)\Bigg\}\\ &2\leqslant i\leqslant NM+1 \end{aligned} \tag{3a}$$

The radiative heat flux at boundary S_1 is

$$\begin{aligned} q_{S_1}^{r}=\sigma\sum_{k=1}^{NB}n_{m,k}^2\Bigg\{&\varepsilon_{2,k}[S_2S_1]_k^{s}A_{k,T_{S_2}}T_{S_2}^4-\varepsilon_{1,k}[S_1S_2]_k^{s}A_{k,T_{S_1}}T_{S_1}^4\\ &+\sum_{j=2}^{NM+1}\left([V_jS_1]_k^{s}A_{k,T_j}T_j^4-\varepsilon_{1,k}[S_1V_j]_k^{s}A_{k,T_{S_1}}T_{S_1}^4\right)\Bigg\} \end{aligned} \tag{3b}$$

The boundary condition at opaque boundary surfaces S_1 is follows:

$$\begin{aligned} q_{S_1}^{r}+2k_2(T_2-T_{S_1})/\Delta x=\sigma\sum_{k=1}^{NB}\left(\varepsilon_{1,k}A_{k,T_{S_1}}T_{S_1}^4-A_{k,T_{S-\infty}}T_{-\infty}^4\right)\\ +h_1\left(T_{S_1}-T_{g_1}\right) \end{aligned} \tag{4}$$

3. Radiative transfer coefficients

The RTC of an element (surface or control volume) i to an element j is defined as the quotient of the radiative energy that is received by the element j in the transfer process of the radiative energy emitted by element i. The radiation transfer process in scattering medium can be divided into two subprocesses [14]. The first subprocess is emitting-attenuating-reflecting subprocess and the RTCs are denoted by $(S_iS_j)_k^{s}$, $(S_iV_j)_k^{s}$, $(V_iV_j)_k^{s}$. The second

subprocess is a multiple absorbing-multiple scattering subprocess and the RTCs are denoted by $[S_iS_j]_k^s$, $[S_iV_j]_k^s$, $[V_iV_j]_k^s$. For convenience, the subscript 'k' of the variables denoting spectral properties and the superscript 's' of the variables denoting specular reflection are omitted in the deductive process in the following text.

The first subprocess can be again divided into the following four steps. (1) Considering the multiple reflection of the surface. (2) The radiative transfer function of the forward scattering and the backward scattering. (3) Considering the incident direction. (4) Considering the scattering direction. For emitting-attenuating-reflecting subprocess, the incident direction of the RTC $(V_{l_2}V_j)$ is denoted by two superscripts. The first superscript denotes the incident direction to control volume l_2 and the second denotes the incident direction to control volume j.

The second subprocess considers the redistributing of the energy quotient in a multiple absorbing-multiple scattering process. The subscripts 'a' and 's' of the RTCs indicate the quotient of absorbing and scattering, respectively.

3.1. Emitting-attenuating-reflecting subprocess

3.1.1. Considering the multiple reflection

(V_iV_j) is used as an example to consider multiple reflection of a surface. There are four kinds of energy transfer paths from the control volume i to the control volume j.

(a) The energy directly reaches j from i and its geometric progression, i.e. energy travels from j to surface S_2, and after being reflected by S_2, the energy reaches surface S_1, and then energy reaches j again (see Fig. 2a).
(b) Energy from i to S_2 is reflected by S_2, then reaches j and its geometric progression (see Fig. 2b).
(c) Energy from i to S_1 is reflected by S_1, then reaches j and its geometric progression (see Fig. 2c).
(d) Energy from i to S_1 is reflected by S_1, reaches S_2, is reflected by S_2 and arrives at j and its geometric progression (see Fig. 2d).

3.1.2. The forward and backward radiative transfer functions

Considering the multi-reflection of the surface and the absorption of the medium, the radiative transfer function $[F^z(z)]$ can be obtained by integral over incident direction (see Figs. 2 and 3):

$$[F^z(z)] = 2\int_0^{\pi/2} \frac{\sin\theta_i\cos\theta_i \exp(-\kappa z/\cos\theta_i)}{1-\rho_1\rho_2\exp(-2\tau_o/\cos\theta_i)}\,\mathrm{d}\theta_i \qquad (5)$$

where $\tau_o = \kappa L$ is the optical thickness; variable z is the normal transfer distance.

For a one-dimensional problem, the scattered energy can be divided into forward scattering and backward scattering direction with respect to the incident direction. Let $\Phi^q(\theta,\theta_i)$ $(0\leqslant\theta\leqslant\pi/2)$ denote the forward scattering phase function and $\Phi^h(\theta,\theta_i)$ $(\pi\leqslant\theta\leqslant-\pi/2)$ denote the backward scattering phase function. According to Bouguer's law and considering the anisotropy of scattering, when radiant intensity taking a trip with a normal displacement of z m after an infinite

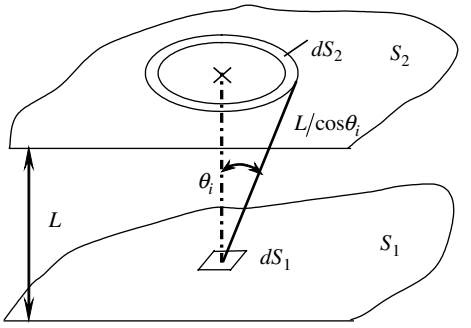

Fig. 3. Sketch of radiative transfer journey between two infinite slabs.

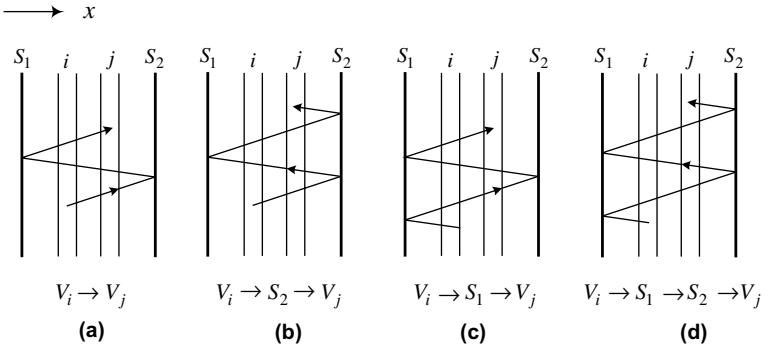

Fig. 2. Sketch of four kinds of transfer paths from the control i to j.

process of the radiative transfer within media on whose surfaces multiple reflection of thermal radiation occurs, the forward and backward radiative transfer functions can be obtained as follows:

$$[F^q(z)] = 2\int_0^{\pi/2} \frac{\sin\theta_i\cos\theta_i \exp(-\kappa z/\cos\theta_i)\frac{1}{\pi/2}\int_0^{\pi/2}\Phi^q(\theta,\theta_i)\,\mathrm{d}\theta}{1-\rho_1\rho_2\exp(-2\tau_o/\cos\theta_i)}\,\mathrm{d}\theta_i \tag{6}$$

$$[F^h(z)] = 2\int_0^{\pi/2} \frac{\sin\theta_i\cos\theta_i \exp(-\kappa z/\cos\theta_i)\frac{1}{\pi/2}\int_\pi^{-\pi/2}\Phi^h(\theta,\theta_i)\,\mathrm{d}\theta}{1-\rho_1\rho_2\exp(-2\tau_o/\cos\theta_i)}\,\mathrm{d}\theta_i \tag{7}$$

Eqs. (6) and (7) denote radiant intensity transfer quotients after the radiant intensity being extincted in the infinite radiative transfer process.

When considering the energy conservation relations:

$$(S_1V_i) = (S_1S_i) - (S_1S_{i+1}) \tag{8}$$

$$(V_iV_j) = (S_{i+1}S_j) - (S_iS_j) - (S_{i+1}S_{j+1}) + (S_iS_{j+1}) \tag{9}$$

The radiative transfer coefficient relative to each transfer path can be obtained:

$$G^z(V_i\to V_j) = F^z(x_{i+1,j}) - F^z(x_{i+1,j+1}) - F^z(x_{i,j}) + F^z(x_{i,j+1}) \tag{10a}$$

$$G^q(V_i\to V_j) = F^q(x_{i+1,j}) - F^q(x_{i+1,j+1}) - F^q(x_{i,j}) + F^q(x_{i,j+1}) \tag{10b}$$

$$G^h(V_i\to V_j) = F^h(x_{i+1,j}) - F^h(x_{i+1,j+1}) - F^h(x_{i,j}) + F^h(x_{i,j+1}) \tag{10c}$$

$$G^p(V_i\to S_1\to V_j) = F^p(x_{i,1}+x_{1,j}) - F^p(x_{i,1}+x_{1,j+1}) - F^p(x_{i+1,1}+x_{1,j}) + F^p(x_{i+1,1}+x_{1,j+1}) \quad (p=z,q,h) \tag{11}$$

$$G^p(V_i\to S_2\to V_j) = F^p(x_{i+1,2}+x_{2,j+1}) - F^p(x_{i+1,2}+x_{2,j}) - F^p(x_{i,2}+x_{2,j+1}) + F^p(x_{i,2}+x_{2,j}) \quad (p=z,q,h) \tag{12}$$

$$G^p(V_i\to S_1\to S_2\to V_j) = F^p(x_{i,1}+L+x_{2,j+1}) - F^p(x_{i,1}+L+x_{2,j}) - F^p(x_{i+1,1}+L+x_{2,j+1}) + F^p(x_{i+1,1}+L+x_{2,j}) \quad (p=z,q,h) \tag{13}$$

3.1.3. Incident direction

For storing the information of the incident direction, the energy radiated into control volume is divided into two parts. One comes from the positive direction of the x-axis (forward direction), the RTC is denoted by superscript 'f' (cf. '1', '2' in Fig. 4). The other comes from the negative direction of x-axis (backward direction), the RTC is denoted by superscript 'b', (cf. '3', '4' in Fig. 4). For example, $(V_iV_{l_2})^f$ is the fraction of emissive power of control volume i, which is radiated into control volume l_2 from the positive direction.

(1) $i < l_2$ (see Fig. 4a)

$$(V_iV_{l_2})^f = G^z(V_i\to V_{l_2}) + \rho_1 G^z(V_i\to S_1\to V_{l_2}) \tag{14a}$$

$$(V_iV_{l_2})^b = \rho_2 G^z(V_i\to S_2\to V_{l_2}) + \rho_1\rho_2 G^z(V_i\to S_1\to S_2\to V_{l_2}) \tag{14b}$$

(2) $i = l_2$ (see Fig. 4b)

$$(V_iV_{l_2})^f = 0.25FV + \rho_1 G^z(V_i\to S_1\to V_{l_2}) + \rho_1\rho_2 G^z(V_i\to S_2\to S_1\to V_{l_2}) \tag{15a}$$

$$(V_iV_{l_2})^b = 0.25FV + \rho_2 G^z(V_i\to S_2\to V_{l_2}) + \rho_1\rho_2 G^z(V_i\to S_1\to S_2\to V_{l_2}) \tag{15b}$$

Here $FV = 4\kappa\Delta x - 2[1-2E_3(\kappa\Delta x)]$ is the direct exchange area of volume i vs volume i [19].

(3) $i > l_2$ (see Fig. 4c)

$$(V_iV_{l_2})^f = \rho_1 G^z(V_i\to S_1\to V_{l_2}) + \rho_1\rho_2 G^z(V_i\to S_2\to S_1\to V_{l_2}) \tag{16a}$$

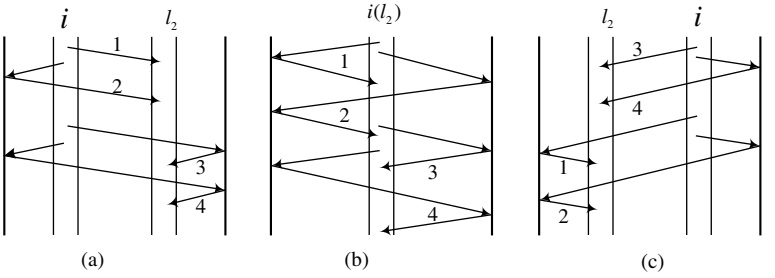

Fig. 4. Radiative transfer direction from the control volume i to l_2. (a) $i < l_2$, (b) $i = l_2$, (c) $i > l_2$.

$$(V_i V_{l_2})^b = G^z(V_i \to V_{l_2}) + \rho_2 G^z(V_i \to S_2 \to V_{l_2}) \tag{16b}$$

The total power entering control volume from both the directions is denoted by superscript 't'.

$$(V_i V_{l_2})^t = (V_i V_{l_2})^f + (V_i V_{l_2})^b$$

3.1.4. Scattering direction

The radiative energy scattered by control volume l_2 is divided into two parts as well. (a) Forward scattering (relative to the incident direction) which is denoted by superscript 'q' for the radiative transfer functions and 'f' for RTC (see Fig. 5). (b) Backward scattering (relative to the incident direction) which is denoted by superscript 'h' for the radiative transfer functions and 'b' for RTC (see Fig. 5). In the following formulas, two superscripts are used in RTC to denote direction of incident radiation into two control-volumes, respectively. The first superscript means the direction of incident radiation into control volume l_2 and the second one means the direction of incident radiation into control volume j, which is scattered by control volume l_2 firstly. We use the superscript 'f' to denote the positively incident direction and use the superscript 'b' to denote the negatively incident direction relative to x-axis. If only considering the incident power into control volume l_2, the second superscript will be 't', and

$$(V_{l_2} V_j)^{ft} = (V_{l_2} V_j)^{ff} + (V_{l_2} V_j)^{fb}$$
$$(V_{l_2} V_j)^{bt} = (V_{l_2} V_j)^{bf} + (V_{l_2} V_j)^{bb}$$

(1) $l_2 < j$, for positive incidence (see Fig. 5a)

$$(V_{l_2} V_j)^{ff} = G^q(V_{l_2} \to V_j) + \rho_1 G^h(V_{l_2} \to S_1 \to V_j) \tag{17a}$$

$$(V_{l_2} V_j)^{fb} = \rho_2 G^q(V_{l_2} \to S_2 \to V_j) + \rho_1 \rho_2 G^h(V_{l_2} \to S_1 \to S_2 \to V_j) \tag{17b}$$

For negative incidence (see Fig. 5b)

$$(V_{l_2} V_j)^{bf} = G^h(V_{l_2} \to V_j) + \rho_1 G^q(V_{l_2} \to S_1 \to V_j) \tag{18a}$$

$$(V_{l_2} V_j)^{bb} = \rho_2 G^h(V_{l_2} \to S_2 \to V_j) + \rho_1 \rho_2 G^q(V_{l_2} \to S_1 \to S_2 \to V_j) \tag{18b}$$

(2) $l_2 = j$, for positive incidence (see Fig. 5c)

$$(V_{l_2} V_j)^{ff} = 0.25FV + \rho_1 G^h(V_{l_2} \to S_1 \to V_j) + \rho_1 \rho_2 G^q(V_{l_2} \to S_2 \to S_1 \to V_j) \tag{19a}$$

$$(V_{l_2} V_j)^{fb} = 0.25FV + \rho_2 G^q(V_{l_2} \to S_2 \to V_j) + \rho_1 \rho_2 G^h(V_{l_2} \to S_1 \to S_2 \to V_j) \tag{19b}$$

For negative incidence (see Fig. 5d)

$$(V_{l_2} V_j)^{bf} = 0.25FV + \rho_1 G^q(V_{l_2} \to S_1 \to V_j) + \rho_1 \rho_2 G^h(V_{l_2} \to S_2 \to S_1 \to V_j) \tag{20a}$$

$$(V_{l_2} V_j)^{bb} = 0.25FV + \rho_2 G^h(V_{l_2} \to S_2 \to V_j) + \rho_1 \rho_2 G^q(V_{l_2} \to S_1 \to S_2 \to V_j) \tag{20b}$$

(3) $l_2 > j$, for positive incidence (see Fig. 5e)

$$(V_{l_2} V_j)^{ff} = \rho_1 G^h(V_{l_2} \to S_1 \to V_j) + \rho_1 \rho_2 G^q(V_{l_2} \to S_2 \to S_1 \to V_j) \tag{21a}$$

$$(V_{l_2} V_j)^{fb} = G^h(V_{l_2} \to V_j) + \rho_2 G^q(V_{l_2} \to S_2 \to V_j) \tag{21b}$$

For negative incidence (see Fig. 5f)

$$(V_{l_2} V_j)^{bf} = \rho_1 G^q(V_{l_2} \to S_1 \to V_j) + \rho_1 \rho_2 G^h(V_{l_2} \to S_2 \to S_1 \to V_j) \tag{22a}$$

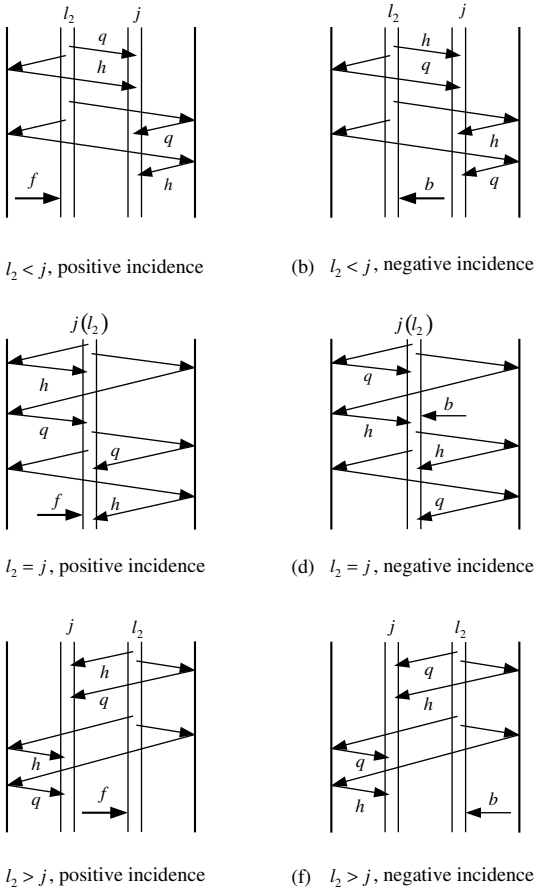

Fig. 5. Sketch of the transfer direction from control volume l_2 scattered to control volume j.

$$(V_{l_2}V_j)^{bb} = G^q(V_{l_2} \to V_j) + \rho_2 G^h(V_{l_2} \to S_2 \to V_j) \tag{22b}$$

3.2. Multiple absorbing-multiple scattering subprocess

The multiple absorbing and scattering in medium are traced until that the transferring energy is reduced to zero. First of all, the RTC must be normalized as follows:

$$(V_iV_j)_k^{*ft} = (V_iV_j)_k^{ft}/(4\kappa_k\Delta x)$$

$$(V_iV_j)_k^{*bt} = (V_iV_j)_k^{bt}/(4\kappa_k\Delta x) \qquad i,\ j = 2\text{–}NM+1$$

$$(V_iS_u)_k^{*f} = (V_iS_u)_k^{f}/(4\kappa_k\Delta x)$$

$$(V_iS_u)_k^{*b} = (V_iS_u)_k^{b}/(4\kappa_k\Delta x) \qquad i = 2\text{–}NM+1$$

$$(S_uV_i)_k^{*} = (S_uV_i)_k/\varepsilon_{u,k} \quad i = 2\text{–}NM+1$$

$$(S_uS_v)_k^{*} = (S_uS_v)_k/\varepsilon_{u,k}$$

where S_u, $S_v = S_1$ or S_2; superscript '*' indicates the normalized parameter.

The detailed deductive process of RTC $[V_iV_j]$ is exemplified as follows. For convenience, the two functions are defined as following:

$$H\left(V_{l_{n+1}}V_{l_n}\right)^{*ft} = \sum_{l_n=2}^{NM+1}\left[\left(V_{l_{n+1}}V_{l_n}\right)^{*ff}H\left(V_{l_n}V_{l_{n-1}}\right)^{*ft} + \left(V_{l_{n+1}}V_{l_n}\right)^{*fb}H\left(V_{l_n}V_{l_{n-1}}\right)^{*bt}\right] \quad n \geqslant 3 \tag{23a}$$

$$H\left(V_{l_{n+1}}V_{l_n}\right)^{*bt} = \sum_{l_n=2}^{NM+1}\left[\left(V_{l_{n+1}}V_{l_n}\right)^{*bf}H\left(V_{l_n}V_{l_{n-1}}\right)^{*ft} + \left(V_{l_{n+1}}V_{l_n}\right)^{*bb}H\left(V_{l_n}V_{l_{n-1}}\right)^{*bt}\right] \quad n \geqslant 3 \tag{23b}$$

If $n = 2$ and the RTC is for the control volume to the control volume, i.e. $(V_iV_j)^{*n\text{th}}$, or the surface to the control volume, i.e. $(S_uV_j)^{*n\text{th}}$, then

$$H(V_{l_3}V_{l_2})^{*ft} = \sum_{l_2=2}^{NM+1}\left[(V_{l_3}V_{l_2})^{*ff}(V_{l_2}V_j)^{*ft} + (V_{l_3}V_{l_2})^{*fb}(V_{l_2}V_j)^{*bt}\right] \tag{24a}$$

$$H(V_{l_3}V_{l_2})^{*bt} = \sum_{l_2=2}^{NM+1}\left[(V_{l_3}V_{l_2})^{*bf}(V_{l_2}V_j)^{*ft} + (V_{l_3}V_{l_2})^{*bb}(V_{l_2}V_j)^{*bt}\right] \tag{24b}$$

If $n = 2$ and the RTC is for the control volume to the surface, i.e. $(V_iS_v)^{*n\text{th}}$, or the surface to the surface, i.e. $(S_uS_v)^{*n\text{th}}$, then

$$H(V_{l_3}V_{l_2})^{*ft} = \sum_{l_2=2}^{NM+1}\left[(V_{l_3}V_{l_2})^{*ff}(V_{l_2}S_v)^{*ft} + (V_{l_3}V_{l_2})^{*fb}(V_{l_2}S_v)^{*bt}\right] \tag{25a}$$

$$H(V_{l_3}V_{l_2})^{*bt} = \sum_{l_2=2}^{NM+1}\left[(V_{l_3}V_{l_2})^{*bf}(V_{l_2}S_v)^{*ft} + (V_{l_3}V_{l_2})^{*bb}(V_{l_2}S_v)^{*bt}\right] \tag{25b}$$

(1) After the first-order scattering

$$[V_iV_j]_{\mathrm{a}}^{*1\mathrm{st}} = (V_iV_j)^{*t}\eta \quad [V_iV_j]_{\mathrm{s}}^{*1\mathrm{st}} = (V_iV_j)^{*t}\omega$$

(2) After the second-order scattering

$$[V_iV_j]_{\mathrm{a}}^{*2\mathrm{nd}} = [V_iV_j]_{\mathrm{a}}^{*1\mathrm{st}} + \sum_{l_2=2}^{NM+1}\left[(V_iV_{l_2})^{*f}(V_{l_2}V_j)^{*ft} + (V_iV_{l_2})^{*b}(V_{l_2}V_j)^{*bt}\right]\omega\eta$$

$$[V_iV_j]_{\mathrm{s}}^{*2\mathrm{nd}} = \sum_{l_2=2}^{NM+1}\left[(V_iV_{l_2})^{*f}(V_{l_2}V_j)^{*ft} + (V_iV_{l_2})^{*b}(V_{l_2}V_j)^{*bt}\right]\omega^2$$

(3) After the third-order scattering

$$\begin{aligned}[V_iV_j]_{\mathrm{a}}^{*3\mathrm{rd}} &= [V_iV_j]_{\mathrm{a}}^{*2\mathrm{nd}} + \sum_{l_3=2}^{NM+1}\left\{(V_iV_{l_3})^{*f}\sum_{l_2=2}^{NM+1}\left[(V_{l_3}V_{l_2})^{*ff}(V_{l_2}V_j)^{*ft} + (V_{l_3}V_{l_2})^{*fb}(V_{l_2}V_j)^{*bt}\right]\right.\\ &\quad \left. + (V_iV_{l_3})^{*b}\sum_{l_2=2}^{NM+1}\left[(V_{l_3}V_{l_2})^{*bf}(V_{l_2}V_j)^{*ft} + (V_{l_3}V_{l_2})^{*bb}(V_{l_2}V_j)^{*bt}\right]\right\}\omega^2\eta\\ &= [V_iV_j]_{\mathrm{a}}^{*2\mathrm{nd}} + \sum_{l_3=2}^{NM+1}\left\{(V_iV_{l_3})^{*f}H(V_{l_3}V_{l_2})^{*ft} + (V_iV_{l_3})^{*b}H(V_{l_3}V_{l_2})^{*bt}\right\}\omega^2\eta\end{aligned}$$

$$[V_iV_j]_{\mathrm{s}}^{*3\mathrm{rd}} = \sum_{l_3=2}^{NM+1}\left\{(V_iV_{l_3})^{*f}H(V_{l_3}V_{l_2})^{*ft} + (V_iV_{l_3})^{*b}H(V_{l_3}V_{l_2})^{*bt}\right\}\omega^3$$

(4) After the $(n+1)$th-order scattering, when $\mathrm{Max}\sum_{j=2}^{NM+1}[V_iV_j]_{\mathrm{s}}^{*(n+1)\mathrm{th}} < \mathrm{EPS0}$, the redistribution of energy is finished:

$$[V_iV_j]_{\mathrm{a}}^{*(n+1)\mathrm{th}} = [V_iV_j]_{\mathrm{a}}^{*n\mathrm{th}} + \sum_{l_{n+1}=2}^{NM+1}\Big[\big(V_iV_{l_{n+1}}\big)^{*f}H\big(V_{l_{n+1}}V_{l_n}\big)^{*ft} + \big(V_iV_{l_{n+1}}\big)^{*b}H\big(V_{l_{n+1}}V_{l_n}\big)^{*bt}\Big]\omega^n\eta \tag{26}$$

$$[V_iV_j]_{\mathrm{s}}^{*(n+1)\mathrm{th}} = \sum_{l_{n+1}=2}^{NM+1}\Big[\big(V_iV_{l_{n+1}}\big)^{*f}H\big(V_{l_{n+1}}V_{l_n}\big)^{*ft} + \big(V_iV_{l_{n+1}}\big)^{*b}H\big(V_{l_{n+1}}V_{l_n}\big)^{*bt}\Big]\omega^{n+1} \tag{27}$$

The other RTCs are given by analogy:

$$[S_uV_j]_{\mathrm{a}}^{*(n+1)\mathrm{th}} = [S_uV_j]_{\mathrm{a}}^{*n\mathrm{th}} + \sum_{l_{n+1}=2}^{NM+1}\Big[\big(S_uV_{l_{n+1}}\big)^{*f}H\big(V_{l_{n+1}}V_{l_n}\big)^{*ft} + \big(S_uV_{l_{n+1}}\big)^{*b}H\big(V_{l_{n+1}}V_{l_n}\big)^{*bt}\Big]\omega^n\eta \tag{28}$$

$$[S_uV_j]_{\mathrm{s}}^{*(n+1)\mathrm{th}} = \sum_{l_{n+1}=2}^{NM+1}\Big[\big(S_uV_{l_{n+1}}\big)^{*f}H\big(V_{l_{n+1}}V_{l_n}\big)^{*ft} + \big(S_uV_{l_{n+1}}\big)^{*b}H\big(V_{l_{n+1}}V_{l_n}\big)^{*bt}\Big]\omega^{n+1} \tag{29}$$

$$[V_iS_v]_{\mathrm{a}}^{*(n+1)\mathrm{th}} = [V_iS_v]_{\mathrm{a}}^{*n\mathrm{th}} + \sum_{l_{n+1}=2}^{NM+1}\Big[\big(V_iV_{l_{n+1}}\big)^{*f}H\big(V_{l_{n+1}}V_{l_n}\big)^{*ft} + \big(V_iV_{l_{n+1}}\big)^{*b}H\big(V_{l_{n+1}}V_{l_n}\big)^{*bt}\Big]\omega^n \tag{30}$$

$$[S_uS_v]_{\mathrm{a}}^{*(n+1)\mathrm{th}} = [S_uS_v]_{\mathrm{a}}^{*n\mathrm{th}} + \sum_{l_{n+1}=2}^{NM+1}\Big[\big(S_uV_{l_{n+1}}\big)^{*f}H\big(V_{l_{n+1}}V_{l_n}\big)^{*ft} + \big(S_uV_{l_{n+1}}\big)^{*b}H\big(V_{l_{n+1}}V_{l_n}\big)^{*bt}\Big]\omega^n \tag{31}$$

After inverse operation and considering $E = 4\kappa_k\eta_k\Delta x$, the RTC for anisotropic scattering is obtained:

$$\begin{aligned}
[V_iV_j]_k &= 4\kappa_k\eta_k\Delta x[V_iV_j]_{\mathrm{a},k}^{*(n+1)\mathrm{th}}\\
[S_uV_j]_k &= \varepsilon_{u,k}[S_uV_j]_{\mathrm{a},k}^{*(n+1)\mathrm{th}}\\
[V_iS_v]_k &= 4\kappa_k\eta_k\Delta x[V_iS_v]_{\mathrm{a},k}^{*(n+1)\mathrm{th}}\\
[S_uS_v]_k &= \varepsilon_{u,k}[S_uS_v]_{\mathrm{a},k}^{*(n+1)\mathrm{th}}
\end{aligned} \tag{32}$$

4. Numerical method and its verification

4.1. Summation relationship of the RTC

The summation relationship of the RTC in anisotropic scattering medium can be expressed as:

$$\sum_{j=2}^{NM+1}[V_iV_j]_k + [V_iS_1]_k + [V_iS_2]_k = 4\kappa_k\eta_k\Delta x \quad i = 2\text{–}NM+1 \tag{33a}$$

$$[S_1S_1]_k + \sum_{j=2}^{NM+1}[S_1V_i]_k + [S_1S_2]_k = \varepsilon_1 \tag{33b}$$

$$[S_2S_1]_k + \sum_{j=2}^{NM+1}[S_2V_i]_k + [S_2S_2]_k = \varepsilon_2 \tag{33c}$$

4.2. Numerical method

Eqs. (6) and (7) are integrated by an adaptive method based on a 30-point Gaussian integration scheme, the integral control precision $\mathrm{EPS3} = 10^{-9}$.

Because the radiative source term and the boundary condition have nonlinear relationship with temperature, both of them must be linearized firstly [20], the linearization of source term is obtained as

$$\Phi_i^{r,m,n+1} = \Phi_i^{r,m,n} + \big(\mathrm{d}\Phi_i^{\mathrm{r}}/\mathrm{d}T_i\big)^{m,n}\big(T_i^{n+1} - T_i^{n}\big)^m \tag{34}$$

where superscript '$n+1$' indicates the $(n+1)$th interation in mth time-step. The TDMA (TriDiagonal Matrix Algorithm) method is applied to solve the linear system of equations, and the control precision $\mathrm{Max}\big|T_i^{m,n+1} - T_i^{m,n}\big| \leqslant \mathrm{EPS1} = 0.001$ K.

4.3. The result of linear anisotropic scattering

Busbridge and Orchard [5] and Maruyama [11] studied the radiative transfer in a pure scattering, gray slab for the case $\omega = 1$, $NB = 1$, $n_m = 1$. Boundary surfaces are black and the temperatures are specified as $T_{S_1} = T_{\mathrm{rf}} = 1000$ K, $T_{S_2} = 0$. The linear anisotropic scattering phase functions are considered as $\Phi_1(\theta,\theta_i) = 1 + 0.5\cos\theta\cos\theta_i$ and $\Phi_2(\theta,\theta_i) = 1 + \cos\theta\cos\theta_i$, respectively. Note Eqs. (3b), (28), (32), since $\eta = 0$, $NB = 1$, $n_m = 1$, $\varepsilon_1 = \varepsilon_2 = 1$ and $T_{S_2} = 0$, the radiative heat flux density at boundary S_1 can be rewritten as:

$$\Big|q_{S_1}^{\mathrm{r}}\Big| = \Big|\sigma\Big\{-[S_1S_2]^{\mathrm{s}}T_{S_1}^4\Big\}\Big| \tag{35}$$

The dimensionless radiative flux $\tilde{q}^{\mathrm{r}}_{\mathrm{Maruyama}}(\tau)$ and the dimensionless reflected radiative flux $\rho^{\mathrm{r}}_{\mathrm{Maruyama}}$ are given as follows (subscript 'Maruyama' indicates the parameters are defined according to Maruyama).

$$\tilde{q}^{\mathrm{r}}_{\mathrm{Maruyama}}(0) = q^{\mathrm{r}}(0)/(\sigma T_{\mathrm{rf}}^4) = |q^{\mathrm{r}}_{S_1}|/\big(\sigma T_{\mathrm{rf}}^4\big) = [S_1S_2]^{\mathrm{s}} \tag{36a}$$

$$\rho^{\mathrm{r}}_{\mathrm{Maruyama}} = 1 - \tilde{q}^{\mathrm{r}}_{\mathrm{Maruyama}}(0) \tag{36b}$$

Since the heat conduction was neglected in Refs. [5,11], therefore, let $k = 1 \times 10^{-14}$ $\mathrm{W\,m^{-1}\,K^{-1}}$ in this paper. Using $\mathrm{EPS0} = 1 \times 10^{-9}$ and $\zeta = 40$–80, the result of comparison with Refs. [5,11] is shown in Table 1.

Machali and Madkour [10] studied the radiative heat transfer in an absorbing and linear-anisotropic pure scattering gray slab for combined specular and diffuse reflection boundaries by the projection method for the case $\omega = 1$ and $n_m = 1$. Boundary surfaces are opaque, gray, and the boundary temperatures are specified as $T_{S_1} = T_{\mathrm{rf}} = 2T_{S_2}$. The dimensionless radiative heat flux is given as follows [subscript 'Machali' indicates that the parameter is defined according to Machali].

$$\begin{aligned}\tilde{q}^{\mathrm{r}}_{\mathrm{Machali}} &= q^{\mathrm{r}}/\left[2\varepsilon_1\sigma T^4_{\mathrm{rf}}\right] = |q^{\mathrm{r}}_{S_1}|/[2\varepsilon_1\sigma T^4_{S_1}] \\ &= |\{[S_2S_1]^{\mathrm{s}}T^4_{S_2} - [S_1S_2]^{\mathrm{s}}T^4_{S_1}\}|/[2T^4_{S_1}]\end{aligned} \tag{37}$$

Table 2 shows the comparison of present result with those of Ref. [10] for the case $k = 1 \times 10^{-14}$ $\mathrm{Wm^{-1}\,K^{-1}}$, $\mathrm{EPS0} = 1 \times 10^{-9}$, $T_{\mathrm{rf}} = T_{S_1} = 1500$ K, $\zeta = 100$. It is shown that the results of this paper are consistent with those in Ref. [10] when $\tau_{\mathrm{o}} \leqslant 1$. But when $\tau_{\mathrm{o}} \geqslant 2$ and $\Phi_2(\theta,\theta_i) = 1 + \cos\theta\cos\theta_i$, $\tilde{q}^{\mathrm{r}}_{\mathrm{Machali}}$ of this paper is greater than those of Ref. [10], and with the increasing of τ_{o} the difference between those increases. When $\tau_{\mathrm{o}} \geqslant 2$ and $\Phi_3(\theta,\theta_i) = 1 - \cos\theta\cos\theta_i$, $\tilde{q}^{\mathrm{r}}_{\mathrm{Machali}}$ of this paper is lesser than those of Ref. [10], and when τ_{o} increases, the difference increases.

When the other parameters are kept unchanged, the results of the different single scattering phase functions must have some inherent relations. For convenience, two functions are defined as follows:

$$\Psi_{12} = \frac{\rho^{\mathrm{r}}_{\mathrm{Maruyama}}[\Phi_1(\theta,\theta_i)]}{\rho^{\mathrm{r}}_{\mathrm{Maruyama}}[\Phi_2(\theta,\theta_i)]} \tag{38}$$

$$\Psi_{23} = \frac{\tilde{q}^{\mathrm{r}}_{\mathrm{Machali}}[\Phi_2(\theta,\theta_i)]}{\tilde{q}^{\mathrm{r}}_{\mathrm{Machali}}[\Phi_3(\theta,\theta_i)]} \tag{39}$$

The results of Ψ_{12} obtained by Busbridge and Orchard [5], Maruyama [11] and this paper are shown in Fig. 6. When $\varepsilon_1 = 0.2$, the results of Ψ_{23} by Machali and Madkour [10] and our model are listed in Table 3. When $\varepsilon_1 = 1$, $\varepsilon_1 = 0.7$ and $\varepsilon_1 = 0.2$, the results of Ψ_{23} by Machali and our model are shown in Fig. 7. It can be seen that the results of this paper seem to be more reasonable than those in the Ref. [10].

4.4. The results of nonlinear anisotropic scattering

Orchard [6] calculated the radiative transfer in a purely nonlinear anisotropic scattering, gray slab, the parameters were: $\omega = 1$, $NB = 1$, $n_m = 1$, $T_{\mathrm{rf}} = T_{S_1} = 1000$ K, $T_{S_2} = 0$, $k = 1 \times 10^{-14}$ $\mathrm{Wm^{-1}\,K^{-1}}$, $\mathrm{EPS0} = 1 \times 10^{-9}$. The dimensionless reflected flux $\rho^{\mathrm{r}}_{\mathrm{Maruyama}}$ was defined in Eqs. (36a) and (36b). Three kinds of nonlinear scattering phase functions are employed in this paper:

$$\Phi_4 = 1 + 0.5\left[\frac{3}{2}(\cos\theta)^2 - \frac{1}{2}\right]\left[\frac{3}{2}(\cos\theta_i)^2 - \frac{1}{2}\right] \tag{40}$$

$$\begin{aligned}\Phi_5 = {} & 1 + \cos\theta\cos\theta_i \\ & + 0.5\left[\frac{3}{2}(\cos\theta)^2 - \frac{1}{2}\right]\left[\frac{3}{2}(\cos\theta_i)^2 - \frac{1}{2}\right]\end{aligned} \tag{41}$$

Table 1
Dimensionless reflected fluxes $\rho^{\mathrm{r}}_{\mathrm{Maruyama}}$ for linear-anisotropic medium with $\omega = 1$, $T_{\mathrm{rf}} = T_{S_1} = 1000$ K, $T_{S_2} = 0$, $\zeta = 40$–80, $n_m = 1$, $\varepsilon_1 = \varepsilon_2 = 1$

τ_{o}	$\Phi_1(\theta,\theta_i) = 1 + 0.5\cos\theta\cos\theta_i$			$\Phi_2(\theta,\theta_i) = 1 + \cos\theta\cos\theta_i$		
	Ref. [5]	Ref. [11]	This paper	Ref. [5]	Ref. [11]	This paper
1	0.4055	0.40674	0.4043754[a]	0.3577	0.36160	0.3556584[a]
			0.4043260[b]			0.3552919[b]
1.2			0.4465705[b]			0.3958174[b]
1.5			0.4995269[b]			0.4476231[b]
2	0.5678	0.56804	0.5681398[a]	0.5154	0.51617	0.5168115[a]
			0.5680838[b]			0.5164068[b]
3	0.6599		0.6607097[b]	0.6102		0.6125566[b]
4	0.7195		0.7205519[b]	0.6738		0.6767364[b]
5	0.7614	0.76143	0.7624812[a]	0.7195	0.71951	0.7229886[a]
			0.7624371[b]			0.7226612[b]
6	0.7923		0.7934004[b]	0.7540		0.7571575[b]
7	0.8162		0.8172225[b]	0.7810		0.7840210[b]
8	0.8351		0.8361188[b]	0.8026		0.8055330[b]
9	0.8505		0.8514739[b]	0.8203		0.8231478[b]
10	0.8633	0.86333	0.8641981[b]	0.8351	0.83512	0.8378365[b]

[a] $\zeta = 40$.
[b] $\zeta = 80$.

Table 2
Comparison of the dimensionless radiative heat fluxes $\tilde{q}^{r}_{\text{Machali}}$ for slabs $\rho_1^d = 0$, $\rho_2^d = 0.2$, $\rho_2^s = 0$, $\varepsilon_2 = 0.8$, $P_{\text{ref}} = 1$, $\omega = 1$, $n_m = 1$, $\zeta = 100$

ε_1		$\tau_o = 0.01$	$\tau_o = 0.1$	$\tau_o = 0.5$	$\tau_o = 1$	$\tau_o = 2$	$\tau_o = 5$
(a) $\Phi_2\ (\theta,\theta_i) = 1 + \cos\theta\cos\theta_i$							
0.2	Ref. [10]	0.44580	0.44055	0.42084	0.39918	0.36008	0.27062
	This paper	0.445854[a]	0.440978[b]	0.422416	0.402770	0.369657	0.297461
0.7	Ref. [10]	0.39720	0.38335	0.33683	0.29299	0.22909	0.13191
	This paper	0.397343[a]	0.384319[b]	0.339727	0.299160	0.242866	0.155902
1.0	Ref. [10]	0.37282	0.35586	0.30168	0.25370	0.18888	0.10124
	This paper	0.372997[a]	0.356935[b]	0.304539	0.259759	0.201875	0.121452
(b) $\Phi_3\ (\theta,\theta_i) = 1 - \cos\theta\cos\theta_i$							
0.2	Ref. [10]	0.44538	0.43649	0.40443	0.37421	0.33032	0.25047
	This paper	0.445319[a]	0.436010[b]	0.402241	0.369110	0.318571	0.226868
0.7	Ref. [10]	0.39602	0.37277	0.30234	0.25005	0.19105	0.11614
	This paper	0.395867[a]	0.371612[b]	0.298426	0.242584	0.177949	0.099421
1.0	Ref. [10]	0.37134	0.34295	0.26315	0.20903	0.15274	0.08791
	This paper	0.371146[a]	0.341579[b]	0.259136	0.201901	0.141122	0.074488

[a] $\zeta = 1000$ (for $\tau_o = 0.01$, $NM = 10$).
[b] $\zeta = 200$ (for $\tau_o = 0.1$, $NM = 20$).

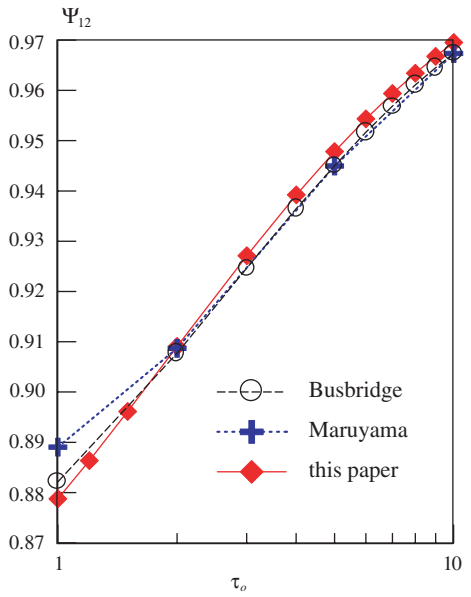

Fig. 6. Ψ_{12} of Busbridge and Orchard [5], Maruyama [11], and this paper ($\zeta = 80$).

$$\Phi_6 = 1 + 1.5\cos\theta\cos\theta_i + 0.5\left[\frac{3}{2}(\cos\theta)^2 - \frac{1}{2}\right]\left[\frac{3}{2}(\cos\theta_i)^2 - \frac{1}{2}\right] \tag{42}$$

With different optical thickness and phase function, $\rho^{r}_{\text{Maruyama}}$ is shown in Table 4. Our results are satisfied with those of Orchard [6]. Define two parameters as follows:

$$\Psi_{54} = \frac{\rho^{r}_{\text{Maruyama}}[\Phi_5(\theta,\theta_i)]}{\rho^{r}_{\text{Maruyama}}[\Phi_4(\theta,\theta_i)]} \tag{43}$$

$$\Psi_{64} = \frac{\rho^{r}_{\text{Maruyama}}[\Phi_6(\theta,\theta_i)]}{\rho^{r}_{\text{Maruyama}}[\Phi_4(\theta,\theta_i)]} \tag{44}$$

The results of Ψ_{54}, Ψ_{64} are shown in Table 5 and Fig. 8.

4.5. The CPU time and precision analyse

The main CPU time of our model is taken to simulate the energy redistribution after scattering. Taking Eq. (26) as an example:

$$[V_iV_j]_a^{*(n+1)\text{th}} = [V_iV_j]_a^{*n\text{th}} + \sum_{l_{n+1}=2}^{NM+1}\Big[\left(V_iV_{l_{n+1}}\right)^{*f}H\left(V_{l_{n+1}}V_{l_n}\right)^{*ft} + \left(V_iV_{l_{n+1}}\right)^{*b}H\left(V_{l_{n+1}}V_{l_n}\right)^{*bt}\Big]\omega^n\eta$$

The calculation is started from the inside to the outside, which is programmed as a subroutine and the calculations performed in pairs (only three loops). So one more scattering will only call two more subroutines. Our ray tracing code runs on PC PIII/1G, and the simulating parameters are: $\omega = 1$, $\zeta = 80$, $\text{EPS0} = 1 \times 10^{-9}$. The total CPU time, which is strongly relative with NUM and the numbers of scattering, is shown in Table 6. The amount of computation for nth scattering is about $n(NM^{3.7} + 4NM^{2.7})$.

4.6. The effect of the number of node on result

The Dimensionless reflected fluxes for different $\zeta = NM/\tau_o$ are shown in Table 7 (also see Tables 1 and 2). It shows that the maximal relative difference between

Table 3
Comparison of results Ψ_{23} when $\varepsilon_1 = 0.2$ ($\rho_1^d = 0$, $\rho_1^s = 0$, $\rho_2^d = 0.2$, $\rho_2^s = 0$, $\varepsilon_2 = 0.2$, $\zeta = 100$)

		$\tau_o = 0.01$	$\tau_o = 0.1$	$\tau_o = 0.5$	$\tau_o = 1$	$\tau_o = 2$	$\tau_o = 5$
Ref. [10]	$\tilde{q}^r_{\text{Machali}}[\Phi_2(\theta,\theta_i)]$	0.44580	0.44055	0.42084	0.39918	0.36008	0.27062
	$\tilde{q}^r_{\text{Machali}}[\Phi_3(\theta,\theta_i)]$	0.44538	0.43649	0.40443	0.37421	0.33032	0.25047
	Ψ_{23}	1.00094	1.00930	1.04058	1.06673	1.09009	1.08045
This paper	$\tilde{q}^r_{\text{Machali}}[\Phi_2(\theta,\theta_i)]$	0.445854[a]	0.440978[b]	0.422416	0.402770	0.369657	0.297461
	$\tilde{q}^r_{\text{Machali}}[\Phi_3(\theta,\theta_i)]$	0.445319[a]	0.436010[b]	0.402241	0.369110	0.318571	0.226868
	Ψ_{23}	1.00120	1.01139	1.05016	1.09119	1.16036	1.31116

[a] $\zeta = 1000$ (for $\tau_o = 0.01$, $NM = 10$).
[b] $\zeta = 200$ (for $\tau_o = 0.1$, $NM = 20$).

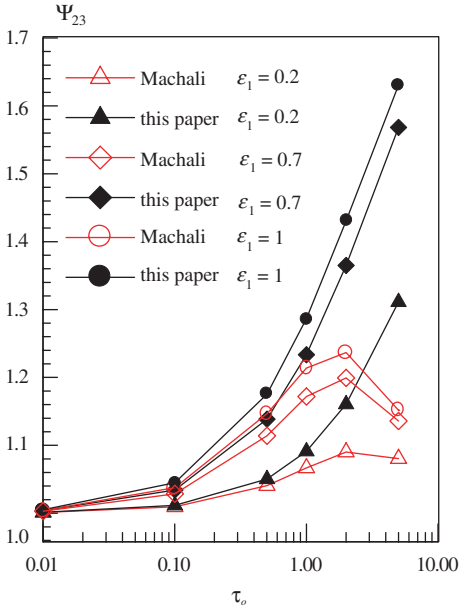

Fig. 7. Ψ_{23} of Machali and Madkour [10] and this paper.

the result of $\zeta = 50$ and that of $\zeta = 60$ is only about 0.0276% ($\Phi_2(\theta,\theta_i), \tau_o = 1$), and with the increase of τ_o, the relative error decrease. So except the comparing calculation with Refs. [5,6,10,11], we take $\zeta = 80$ or 100, in all other calculation, we let $\zeta = 50$.

5. Transient heat transfer for specified boundary temperature

Consider the semi-transparent gray slab with opaque boundaries and hold an initial condition of a uniform temperature distribution (T_0). One boundary is suddenly fixed at the temperature T_{S_2} and the others are kept at temperature T_0 by setting $h_1 = h_2 = \infty = 1 \times 10^{25}$ W m^{-2} K^{-1}, up to the steady-state, and $T_0 = T_{S_1} = T_{g1} = 750$ K, $T_{\text{rf}} = T_{S_2} = T_{g2} = 1500$ K. The other parameters are taken as $L = 0.1$ m, $NB = 1$, $n_m = 1$, $\kappa = 50$ or 100, $\rho_1 = \rho_2 = 0$ or 0.9, $\omega = 0.5$ or 0.9, $Np = 0.005$, $H_1 = H_2 = 5.2261 \times 10^{22}$. The following isotropic scattering and linear anisotropic scattering phase functions are considered.

Table 4
Dimensionless reflected fluxes ρ^r_{Maruyama} for nonlinear-anisotropic medium at $\omega = 1$ $T_{\text{rf}} = T_{S_1} = 1000$ K, $T_{S_2} = 0$, $\zeta = 80$, $n_m = 1$, $\varepsilon_1 = \varepsilon_2 = 1$

τ_o	Φ_4		Φ_5		Φ_6	
	Ref. [6]	This paper	Ref. [6]	This paper	Ref. [6]	This paper
1	0.4468	0.4424437 0.4424567[a]	0.3580	0.3513212	0.3020	0.2939539
2	0.6101	0.6052842 0.6052956[a]	0.5157	0.5113866	0.4490	0.4458478
3	0.6985	0.6939824	0.6104	0.6075034	0.5437	0.5433448
4	0.7541	0.7500593	0.6739	0.6719365	0.6104	0.6115764
5	0.7924	0.7887545	0.7197	0.7181824	0.6601	0.6620517
6	0.8204	0.8170720	0.7541	0.7529978	0.6985	0.7009137
7	0.8417	0.8386944	0.7810	0.7801561	0.7292	0.7317588
8	0.8585	0.8557454	0.8026	0.8019337	0.7541	0.7568364
9	0.8721	0.8695361	0.8204	0.8197856	0.7749	0.7776258
10	0.8833	0.8809202	0.8352	0.8346855	0.7924	0.7951404

[a] $\zeta = 160$.

Table 5
Comparison of results Ψ_{54} and Ψ_{64} ($\zeta = 80$)

τ_o	$\Psi_{54} = \frac{\rho^r_{Maruyama}[\Phi_5(\theta,\theta_i)]}{\rho^r_{Maruyama}[\Phi_4(\theta,\theta_i)]}$		$\Psi_{64} = \frac{\rho^r_{Maruyama}[\Phi_6(\theta,\theta_i)]}{\rho^r_{Maruyama}[\Phi_4(\theta,\theta_i)]}$	
	Ref. [6]	This paper	Ref. [6]	This paper
1	0.80125	0.79405	0.67592	0.65791
2	0.84527	0.84487	0.73594	0.73659
3	0.87387	0.87539	0.77838	0.78294
4	0.89365	0.89584	0.80944	0.81537
5	0.90825	0.91053	0.83304	0.83936
6	0.91919	0.92158	0.85141	0.85784
7	0.92788	0.93020	0.86634	0.87250
8	0.93489	0.93712	0.87839	0.88442
9	0.94072	0.94279	0.88854	0.89430
10	0.94555	0.94752	0.89709	0.90262

$$\Phi_0(\theta,\theta_i) = 1$$
$$\Phi_2(\theta,\theta_i) = 1 + \cos\theta\cos\theta_i$$
$$\Phi_3(\theta,\theta_i) = 1 - \cos\theta\cos\theta_i \quad (45)$$

Let $D\Theta$ be the difference of dimensionless temperature, and

$$D\Theta_{20} = \Theta(\Phi_2) - \Theta(\Phi_0) = \frac{T(\Phi_2) - T(\Phi_0)}{T_{rf} - T_0} \quad (46a)$$

$$D\Theta_{30} = \Theta(\Phi_3) - \Theta(\Phi_0) = \frac{T(\Phi_3) - T(\Phi_0)}{T_{rf} - T_0} \quad (46b)$$

Transient temperatures are shown in Figs. 9–12 for the case $\Delta t^* = 0.001$, EPS0 $= 1 \times 10^{-9}$, $\zeta = 50$.

When $\tau_o = 5$ and $\varepsilon_1 = \varepsilon_2 = 1$, the difference of transient dimensionless temperature distributions $D\Theta_{20}$ and $D\Theta_{30}$, which show symmetry character, are shown in Fig. 9. The extremums of them are shown in Table 8. For $\tau_o = 10$ and $\varepsilon_1 = \varepsilon_2 = 1$, the difference of transient dimensionless temperature distributions $D\Theta_{20}$ and $D\Theta_{30}$ are shown in Fig. 10. All results indicate that with the increasing of the optical thickness, when $t^* = 0.8$, the difference of transient temperature distributions increases, when $t^* = t^*_s$, the difference of temperature distributions decrease.

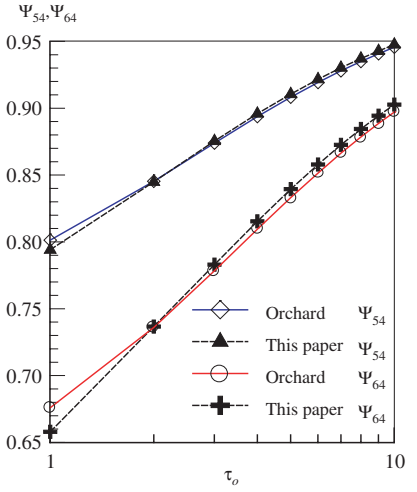

Fig. 8. Ψ_{54}, Ψ_{64} of Orchard [6] and this paper.

In absorbing, emitting and scattering simulation, when the reflectivity of the surface is not zero, radiative energy undergoes multi-scattering by medium and

Table 6
The CPU time

τ_o	$\Phi_1(\theta,\theta_i) = 1 + 0.5\cos\theta\cos\theta_i$			$\Phi_2(\theta,\theta_i) = 1 + \cos\theta\cos\theta_i$		
	nth scattering	NM	CPU time	nth scattering	NM	CPU time
2	81	160	179 s	76	160	170 s
3	128	240	21 min 25 s	118	240	19 min 43 s
4	185	320	92 min	167	320	82 min 7 s
5	251	400	276 min	224	400	246 min

Table 7
Dimensionless reflected fluxes $\rho^r_{Maruyama}$ for different $\zeta = NM/\tau_o$

$\zeta = NM/\tau_o$	$\Phi_1(\theta,\theta_i) = 1 + 0.5\cos\theta\cos\theta_i$		$\Phi_2(\theta,\theta_i) = 1 + \cos\theta\cos\theta_i$	
	$\tau_o = 1$	$\tau_o = 3$	$\tau_o = 1$	$\tau_o = 3$
10	0.4041492	0.6606801	0.3571997	0.6146590
20	0.4043971	0.6608098	0.3562913	0.6136236
40	0.4043754	0.6607627	0.3556584	0.6129429
50	0.4043588	0.6607439	0.3555160	0.6127923
60	0.4043454	0.6607296	0.3554180	0.6126890
80	0.4043260	0.6607097	0.3552919	0.6125566
100	0.4043129	0.6606966	0.3552142	0.6124753
150	0.4042937	0.6606780	0.3551083	0.6123648

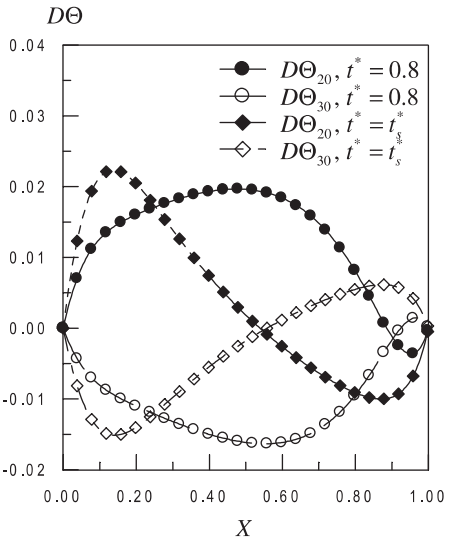

Fig. 9. Relative temperature difference distributions between anisotropic scattering and isotropic scattering media for $\tau_o = 5$, $\varepsilon_1 = \varepsilon_2 = 1$, $\omega = 0.9$.

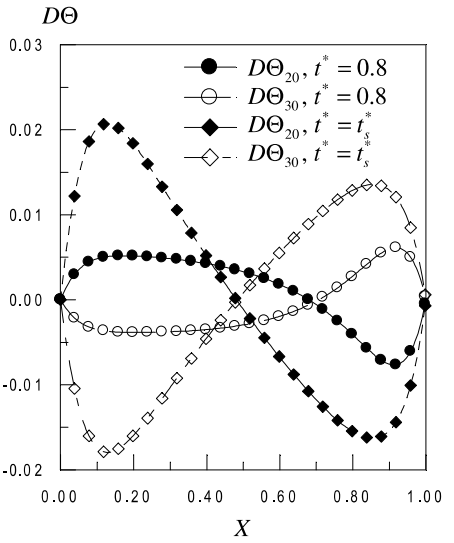

Fig. 11. Relative temperature difference distributions between anisotropic scattering and isotropic scattering media for $\tau_o = 5$, $\varepsilon_1 = \varepsilon_2 = 0.1$, $\omega = 0.9$.

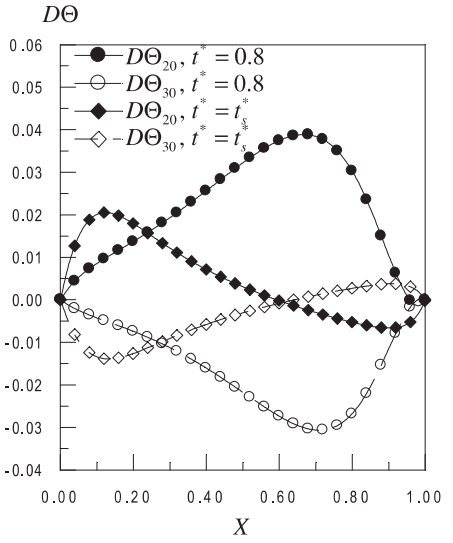

Fig. 10. Relative temperature difference distributions between anisotropic scattering and isotropic scattering media for $\tau_o = 10$, $\varepsilon_1 = \varepsilon_2 = 0.1$, $\omega = 0.9$.

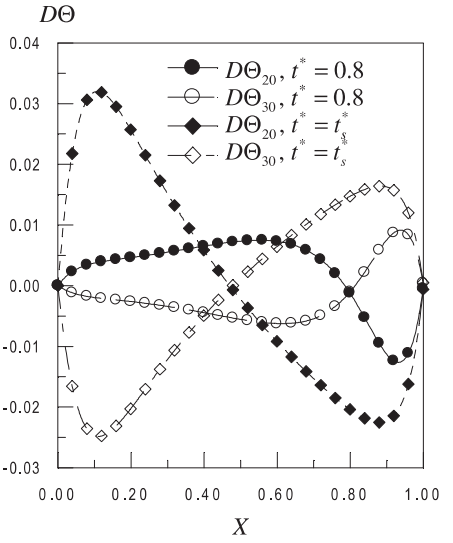

Fig. 12. Relative temperature difference distributions between anisotropic scattering and isotropic scattering media for $\tau_o = 10$, $\varepsilon_1 = \varepsilon_2 = 0.1$, $\omega = 0.9$.

Table 8
The extremum of temperature difference and the extreme point

τ_o	t^*	$\varepsilon_1 = \varepsilon_2 = 1$			$\varepsilon_1 = \varepsilon_2 = 0.1$	
		$D\Theta_{20}$	$T(\Phi_2) - T(\Phi_0)$ [K]	$D\Theta_{30}$	$D\Theta_{20}$	$D\Theta_{30}$
5	0.8	0.01965	14.74	−0.01633	−0.00766	0.00611
	t_s^*	0.02236	16.77	−0.01512	0.02073	−0.01795
10	0.8	0.03883	29.12	−0.03067	−0.01264	0.00913
	t_s^*	0.02052	15.39	−0.01391	0.03197	−0.02485

multi-reflecting by the surface before being absorbed by the medium and the surfaces. The results in Figs. 9–12 indicate that, the difference among the results for three kinds of phase functions decreases with an increase of reflectivity. It is explained as that for opaque boundary surfaces, an increase of reflectivity predicates a decrease of emissivity, and with the decrease of emissivity, the contribution of surface radiation to temperature fields inside the media decreases, which results in the decrease of the temperature difference between the anisotropic scattering and the isotropic scattering media.

6. Conclusions

A model was developed by using the ray tracing method in combination with the nodal analysis for solving the coupled radiative and conductive heat transfer in an anisotropic scattering medium. On the basis of the two sub-processes from the radiative transfer process, the RTCs for a one-dimensional anisotropic scattering nongray slab with two opaque, specular reflective boundaries were deduced. The temperature distributions and radiative fluxes were obtained for the boundary conditions of external radiation and convection.

Numerical analysis in the present study leads to the following summaries:

(1) There are many papers about the anisotropic scattering, but most of them lacked some calculating parameters for comparison. The present results were compared with those from the exact solution [5], REM^2 [11], and projection method [10]. It is shown that some differences exist between the present results and those of Machali. When $\tau_o \leqslant 1$, the results of this paper agree very well with those of [10]. When $\tau_o > 1$ and $\Phi(\mu, \mu_i) = 1 + \mu\mu_i$, the results of this paper are greater than those of [10]. When $\tau_o > 1$ and $\Phi(\mu, \mu_i) = 1 - \mu\mu_i$, the results of this paper are lesser than those of Machali and Madkour, and difference between them increases with the increase of τ_o. So we think that the results of [10] have some error.

(2) It is found that the ratio of two-dimensionless heat fluxes with two different scatting phase function is a monotonous function of optical thickness, for instance Ψ_{12}, Ψ_{23}, Ψ_{54} and Ψ_{64} defined in Eqs. (38), (39), (43) and (44), respectively (see Figs. 6–8). It can be used to verify the calculating result.

(3) Under the condition considered in this paper, the influence of anisotropic scattering on temperature field is small, the temperature differences of forward and backward scattering are about 20 K comparing with the results of isotropic scattering, but the effects of anisotropic scattering on heat flux are larger than those on temperature field.

Acknowledgements

This research is financially supported by the key program of the National Natural Science Foundation of China (Grant No. 50336010), the China National Key Basic Research Special Funds (Grant No. 2003CB214500), and the Research Foundation for the Doctoral Program of Higher Education of China (Grant No. 20030213024).

References

[1] U. Heinemann, R. Caps, J. Fricke, Radiation–conduction interaction: an investigation on silica aerogels, Int. J. Heat Mass Transfer 39 (10) (1996) 2115–2130.
[2] R. Siegel, Temperature distributions in channel walls with translucent thermal barrier coatings, AIAA J. Thermophys. Heat Transfer 12 (3) (1998) 289–296.
[3] R. Siegel, Transient thermal analysis of a translucent thermal barrier coating on a metal wall, ASME J. Heat Transfer 121 (2) (1999) 478–481.
[4] V.A. Petrov, Combined radiation and conduction heat transfer in high temperature fiber thermal insulation, Int. J. Heat Mass Transfer 40 (1997) 2241–2247.
[5] I.W. Busbridge, S.E. Orchard, Reflection and transmission of light by a thick atmosphere according to a phase function: $1 + x\cos\theta$, Astrophys. J. 149 (1967) 655–664.
[6] S.E. Orchard, Reflection and transmission of light by thick atmospheres of pure scattering with a phase function: $1 + \omega_1 P_1(\cos\theta) + \omega_2 P_2(\cos\theta)$, Astrophys. J. 149 (1967) 665–674.
[7] W.W. Yuen, L.W. Wong, Heat transfer by conduction and radiation in a one-dimensional absorbing, emitting and anisotropically scattering medium, ASME J. Heat Transfer 102 (2) (1980) 303–307.
[8] J.H. Tsai, J.D. Lin, Transient combined conduction and radiation with anisotropic scattering, AIAA J. Thermophys. Heat Transfer 4 (1) (1990) 92–97.
[9] C.E. Siewert, An improved iterative method for solving a class of coupled conductive–radiative heat transfer problems, J. Quant. Spectosc. Radiat. Transfer 54 (4) (1995) 599–605.
[10] H.F. Machali, M.A. Madkour, Radiative transfer in a participating slab with anisotropic scattering and general boundary conditions, J. Quant. Spectrosc. Radiat. Transfer 54 (5) (1995) 803–813.
[11] S. Maruyama, Radiative heat transfer in anisotropic scattering media with specular boundary subjected to collimated irradiation, Int. J. Heat Mass Transfer 41 (18) (1998) 2847–2856.
[12] C.C. Liu, R.L. Dougherty, Anisotropically scattering media having a reflective upper boundary, J. Thermophys. Heat Transfer 13 (2) (1999) 177–184.
[13] H.-P. Tan, M. Lallemand, Transient radiative-conductive heat transfer in flat glasses submitted to temperature, flux and mixed boundary conditions, Int. J. Heat Mass Transfer 32 (5) (1989) 795–810.
[14] H.-P. Tan, T.W. Tong, L.-M. Ruan, X.-L. Xia, Q.-Z. Yu, Transient coupled radiative and conductive heat

transfer in an absorbing, emitting and scattering medium, Int. J. Heat Mass Transfer 42 (15) (1999) 2967–2980.

[15] H.-P. Tan, P.-Y. Wang, X.-L. Xia, Transient coupled radiation and conduction in an absorbing and scattering composite layer, AIAA J. Thermophys. Heat Transfer 14 (1) (2000) 77–87.

[16] J.-F. Luo, X.-L. Xia, H.-P. Tan, T.W. Tong, Transient coupled heat transfer in three-layer composite with opaque specular surfaces, AIAA J. Thermophys. Heat Transfer 16 (3) (2002) 297–305.

[17] H.-P. Tan, J.-F. Luo, X.-L. Xia, Transient coupled radiation and conduction in a three-layer composite with semitransparent specular interfaces and surfaces, ASME J. Heat Transfer 124 (3) (2002) 470–481.

[18] J.B. Saulnier, La modélisation thermique et ses applications aux transferts couplés et au contrôle actif, Thèse de Doctorat d'Etat, Université de Poitiers, France,1980.

[19] H.C. Hottel, A.F. Sarofim, Radiative Transfer, McGraw-Hill Book Company, New York, 1967.

[20] S.V. Patankar, Numerical Heat Transfer and Fluid Flow, McGraw-Hill Book Company, New York, 1980.